HHS Public Access

Author manuscript

J Neural Eng. Author manuscript; available in PMC 2020 June 23.

Published in final edited form as:

J Neural Eng. 2019 February ; 16(1): 016007. doi:10.1088/1741-2552/aaeb0c.

On the parameters used in finite element modeling of compound peripheral nerves

Nicole A Pelot[1], **Christina E Behrend**[1], **Warren M Grill**[1,2,3,4]

[1]Duke University, Department of Biomedical Engineering, Room 1427, Fitzpatrick CIEMAS, 101 Science Drive, Campus Box 90281, Durham, NC 27708

[2]Duke University, Department of Electrical and Computer Engineering, Durham, NC, USA

[3]Duke University, Department of Neurobiology, Durham, NC, USA

[4]Duke University School of Medicine, Department of Neurosurgery, Durham, NC, USA

Abstract

Objective.—Computational modeling is an important tool for developing and optimizing implantable neural stimulation devices, but requires accurate electrical and geometrical parameter values to improve predictive value. We quantified the effects of perineurial (resistive sheath around each fascicle) and endoneurial (within each fascicle) parameter values for modeling peripheral nerve stimulation.

Approach.—We implemented three-dimensional finite element models of compound peripheral nerves and cuff electrodes to quantify activation and block thresholds of model axons. We also implemented a two-dimensional finite element model of a bundle of axons to estimate the bulk transverse endoneurial resistivity; we compared numerical estimates to an analytical solution.

Main results.—Since the perineurium is highly resistive, potentials were approximately constant over the cross section of a fascicle, and the perineurium resistivity, longitudinal endoneurial resistivity, and fascicle diameter had important effects on thresholds. Activation thresholds increased up to ~130% for higher perineurium resistivity (~400 vs. 2200 Ω-m) and by ~35–250% for lower longitudinal endoneurial resistivity (3.5 vs. 0.75 Ω-m), with larger increases for smaller diameter axons and for axons in larger fascicles. Further, thresholds increased by ~30–180% for larger fascicle radii, yielding a larger increase with higher perineurium resistivity. Thresholds were largely insensitive to the transverse endoneurial resistivity, but estimates of the bulk resistivity increased with extracellular resistivity and axonal area fraction; the numerical and analytical estimates were in strong agreement except at high axonal area fractions, where structured axon placements that achieved tighter packing produced electric field inhomogeneities.

Significance.—We performed a systematic investigation of the effects of values and methods for modeling the perineurium and endoneurium on thresholds for neural stimulation and block. These results provide guidance for future modeling studies, including parameter selection, data interpretation, and comparison to experimental results.

warren.grill@duke.edu.

Keywords

neural computational modeling; peripheral nerve stimulation; finite element method; neuroengineering; neural engineering; vagus nerve stimulation

1. Introduction

Development of implantable devices delivering electrical stimulation to the nervous system to treat diseases and disorders has accelerated with improved technologies and with increased understanding of the effects of electrical stimulation on the nervous system. Computational models are an important tool for advancing and optimizing these therapies; they contribute to improved electrode designs and stimulation parameters, e.g., (Briaire and Frijns, 2006; Butson et al., 2011; Howell et al., 2015; Wongsarnpigoon and Grill, 2010), and to increased understanding of mechanisms of action, e.g., (Feng et al., 2014; Lempka et al., 2015; McGee and Grill, 2016; Pelot et al., 2017). The two-step process described in McNeal's seminal paper (McNeal, 1976) has been used extensively to model extracellular neural stimulation, e.g., (Choi et al., 2001; Lempka et al., 2015; Schiefer et al., 2008). The first step requires calculation of the distribution of electric potentials generated in the tissue by a voltage or current source. In the second step, the potentials are spatially sampled and applied as extracellular potentials to a cable model of a neuron. The potentials may be computed analytically for simple electrode geometries or numerically, e.g., using a finite element model (FEM), for more complex geometries. The results, including the potential distribution and resulting activation or block thresholds, depend on the morphological and electrical parameters used to represent the tissue and electrodes.

One application of these modeling techniques is the study of stimulation of compound peripheral nerves. There is widespread interest in electrical stimulation and block of peripheral autonomic nerves to treat various diseases and disorders, including obesity, rheumatoid arthritis, heart failure, and bladder dysfunction (Birmingham et al., 2014; Famm et al., 2013), and of peripheral motor nerves to control motor function (Bhadra and Peckham, 1997). A compound nerve is comprised of fascicles ensheathed in perineurium and embedded in epineurium; each fascicle is comprised of a bundle of axons in endoneurial connective tissue (Figure 1).

The perineurium is highly resistive and very thin. More specifically, the impedance of the perineurium was measured for frog sciatic nerves across a range of frequencies (Weerasuriya et al., 1984) and the perineurial thickness is proportional to the fascicle diameter (Grinberg et al., 2008). However, the parameters typically used to represent the perineurium in published models have not acknowledged contributions of geometry, resistivity, frequency, and temperature. Further, the perineurium strongly influences the distribution of potentials in the nerve, and axons within smaller fascicles have lower activation thresholds than axons in larger fascicles. However, the mechanisms underlying this phenomenon are not clear.

Typically, a homogenized anisotropic resistivity is assigned to the fascicular tissue within the perineurium (i.e., the bulk endoneurium), rather than modeling the constituent tissues. Obtaining accurate measurements of the bulk endoneurial resistivity is challenging and

focused on bundles of myelinated axons (Altman and Plonsey, 1989; Nicholson, 1965; Ranck and Bement, 1965; Tasaki, 1955). Certain applications, such as abdominal vagus nerve stimulation for treatment of obesity, rely on stimulation of a nerve nearly completely comprised of unmyelinated axons (Martin-Portugues, 2005; Robinson, 1972; Sarr et al., 2012). Bulk resistivity measurements for an isolated fascicle with unmyelinated axons are lacking in literature, despite the growing interest in development of therapies employing stimulation or block of autonomic nerves.

In this paper, we implemented volume conductor models of peripheral nerve stimulation (nerve and cuff electrode) using the finite element method and coupled the resulting potentials to biophysically-realistic model axons. We used the model to quantify the effects of FEM parameters, including the representation and parameters of the perineurium and the transverse and longitudinal resistivities of the endoneurium, on thresholds for nerve fibre activation and block. Herein we provide a critical examination of the electrical and geometrical parameters used in computational modeling of peripheral nerve stimulation, integrating literature review and original simulations. We highlight factors that must be considered in measuring and using these parameters (such as temperature, frequency, and nerve morphology and ultrastructure), and we quantify which parameters have a greater (e.g., fascicle size, perineurium resistivity, longitudinal endoneurial resistivity) or lesser (e.g., transverse endoneurial resistivity, axon location within a fascicle) impact on thresholds for activation and block. Thus, these findings provide an important resource for conducting computational modeling studies, including selecting model parameters, interpreting model results, and addressing discrepancies between modeling and experimental data. Further, the results inform future measurements of tissue properties. Finally, highlighting the effects of FEM parameters on current flow and on neural activation and block informs data interpretation and therapeutic translation by revealing parameters that might differ between experiments and individuals, as well as across species, which could impact neural responses to stimulation.

2. Methods

2.1. Three-Dimensional Finite Element Models of Nerves and Cuff Electrodes

We implemented FEMs of a compound peripheral nerve and cuff electrode in COMSOL Multiphysics v5.3 (Burlington, MA) (Figure 2) with the geometrical and electrical parameters outlined in Table 1. The first nerve model used a simplified geometry, where the nerve was a cylinder of epineurium containing one or two cylindrical fascicles. We based the range of fascicle radii on the human vagus nerve at upper thoracic spinal levels (0.3 mm) (Kawagishi et al., 2008) and on our own cadaveric samples of the human subdiaphragmatic vagus nerve (0.1 mm). The second nerve model represented realistic human vagus nerve morphology, containing 10 fascicles; we drew their radii from a uniform random distribution from 0.05 to 0.3 mm and randomly placed them using disk point picking, except for the first two fascicles, where the first fascicle was centred and sized to r_{fasc} = 0.1 or 0.3 mm, and the second fascicle was placed at (x_{fasc}, y_{fasc}) = (0.5, 0.5) mm with r_{fasc} = 0.3 mm, to mimic the simplified model. We required at least 75 μm between any two fascicle boundaries and any

fascicle boundary and the nerve boundary. The 10 fascicles covered 25% of the nerve cross-sectional area with r_{fasc} = 0.3 mm for the centre fascicle and 21.4% with r_{fasc} = 0.1 mm.

We evaluated two cuff electrode designs (Figure 2): a monopolar partial cuff and a bipolar circumneural cuff. We evaluated both designs on the simplified nerve model; we used the bipolar circumneural cuff on the multifascicular nerve model. For both cuff designs, the entire electrode was surrounded by a uniform layer of encapsulation tissue (150 μm thick) (Haberler et al., 2000; Moss et al., 2004) and the boundaries of the electrode substrate with the encapsulation tissue were insulating ($\vec{J} \cdot \hat{n} = 0$). We placed the nerve and electrode in a homogeneous isotropic fatty medium with all outside surfaces grounded. We also filled the space between the nerve and cuff with fat.

We based the monopolar partial cuff design on the electrode used for vBloc® therapy by ReShape Lifesciences Inc. (previously EnteroMedics Inc.; St. Paul, MN) (Camilleri et al., 2008; Foster et al., 2010) (Table 1). We represented 75 μm of the extraneural fatty medium between the nerve and the encapsulation tissue to prevent a singularity when assembling and meshing the geometry. We assigned 1 V to the active electrode and integrated the current density over the grounded outer surfaces of the model to determine the total applied current; when using a monopolar source, this source implementation is equivalent to the boundary current source described below (Pelot et al., 2018).

The contacts of the bipolar circumneural cuff were 1 mm long and spaced 1 mm apart edge-to-edge, with an additional 1 mm of insulator at each end (5 mm total cuff length). The cuff was 1 mm thick with an inner diameter of 3.45 mm, placed around a 3 mm diameter nerve. We assigned a boundary current source (i.e. current density) to each electrode contact: 1 mA divided by the surface area for one contact and −1 mA divided by the surface area for the other.

We generated an FEM mesh of the simplified nerve with the monopolar cuff geometry using triangular prism elements; specifically, we created a 2D mesh with triangular elements on one end of the cylindrical model, and swept the mesh to the other end. We generated an FEM mesh of the simplified and multifascicular nerves with the bipolar cuff geometry using a free tetrahedral mesh. While all models were ultimately solved in COMSOL v5.3, the former model was originally built in an earlier version of the software where the swept mesh was more stable. We used cubic and quadratic geometric shape functions for the simplified and multifascicular nerve models, respectively, to reduce the computational demands of the multifascicular nerve model; we used quadratic solution shape functions for all models. We verified that increasing the size of the surrounding volume or the number of domain elements resulted in <2% change in cathodic activation thresholds for a 2 μm axon centred in each of the smaller fascicles (more stringent mesh requirements), resulting in 943,296 elements with the monopolar partial cuff and 9,192,590 elements with the bipolar circumneural cuff for the simplified model; the multifascicular nerve model had 10,025,266 elements with the larger centre fascicle and 9,981,285 with the smaller centre fascicle. We used the conjugate gradients solver to solve Laplace's equation, assuming quasi-static conditions and non-dispersive materials (Bossetti et al., 2008):

$$\nabla \cdot (\sigma \cdot \nabla \phi) = 0 \quad (1)$$

2.2. Biophysically-Realistic Axon Model

We applied the electric potentials from the FEM to 100 mm-long model axons in NEURON v7.3 (Carnevale and Hines, 2006). Specifically, we used the 2 and 10 μm diameter myelinated mammalian McIntyre-RichardsonGrill (MRG) model axons (McIntyre et al., 2002, 2004). We initialized each simulation with 10 ms time steps from t = −200 ms to t = 0 ms to ensure initial steady-state, and ran each simulation from t = 0 ms to 10 ms with 5 μs time steps using backward Euler integration. All threshold values were obtained for a 0.1 ms cathodic (negative) pulse using a binary search algorithm with a resolution of 1%.

2.3. Modeling the Perineurium

We modeled each fascicle as bulk anisotropic endoneurium (homogenized equivalent of a bundle of axons in connective tissue) surrounded by a perineurial sheath. Accurate modeling of the thin (~10 μm) and highly resistive perineurium is important for calculating accurate stimulation thresholds (Grinberg et al., 2008). The perineurium can be modeled either as a thin meshed layer by specifying the resistivity or by using a “contact impedance” boundary condition by specifying the sheet resistance. The former approach is more realistic, but computationally demanding given the large number of very small mesh elements required to describe such a thin layer. We compared the thresholds for model nerve fibre activation and block with different representations of the perineurium (Table 2).

Rather than specifying the resistivity of a thin layer, the sheet resistance can instead be specified as the product of the resistivity ($\rho = 1/\sigma$) and the layer’s thickness (d):

$\vec{J} = \sigma \vec{E}$	Ohm’s law (constitutive relation)
$\vec{J} = -\sigma \nabla \phi$	Substitute scalar potential for electric field
$\vec{n} \cdot \vec{J} = \vec{n} \cdot (-\sigma \nabla \phi)$	Normal component
$\vec{n} \cdot \vec{J} = -\sigma\left(\frac{\partial \phi}{\partial r}\right)$	Assuming that the unit normal vector is pointed radially
$\vec{n} \cdot \vec{J} = -\sigma\left(\frac{\Delta \phi}{\Delta r}\right) = -\frac{\sigma}{d}\Delta \phi$	Assuming d is small, such that the electric field is constant
$\vec{n} \cdot \vec{J_2} = -\frac{\sigma}{d}(V_1 - V_2) = \frac{\sigma}{d}(V_2 - V_1)$	Unit normal vector points outward from medium 2
$\vec{n} \cdot \vec{J_2} = \left(\frac{1}{R_S}\right)(V_2 - V_1)$	Specify sheet resistance, Rs, in Ω-m^2 (“contact impedance” boundary condition in COMSOL)

We surveyed representations of the perineurium in computational models in literature (Supplement A) and selected different values for the perineurium resistance as follows (Table 2):

i. **Weerasuriya, DC, room temp (21°C)**: Weerasuriya (Weerasuriya et al., 1984) measured the impedance of the perineurium of the monofascicular frog sciatic nerve. They reported **0.0478 Ω-m^2** at DC (0 Hz) and at room temperature.[1] This

value is in widespread use for compound nerve modeling, although implementations vary (Supplement A).

ii. **Weerasuriya, DC, 37°C**: Weerasuriya performed measurements at "room temperature", which previous investigators assumed to mean 21°C. To account for the effect of temperature on resistivity, we can adjust the conductivity using a Q_{10} factor (Frieswijk et al., 1998; Raspopovic et al., 2017), resulting in a sheet resistance of **0.0250 Ω-m^2**.

$$R_{S,37oC} = \left[\left(\frac{1}{R_{S,21oC}}\right) * Q_{10}^{\frac{\Delta T\, in\, degC}{10}}\right]^{-1} = \left[\left(\frac{1}{0.0478\,\Omega \cdot \mathrm{m}^2}\right) * (1.5)^{\frac{37-21}{10}}\right]^{-1} = 0.0250\,\Omega \cdot \mathrm{m}^2$$

i. **Weerasuriya, 10 kHz, room temp**: Weerasuriya performed measurements from 2 Hz to 100 kHz, and fit their data to four different equivalent lumped circuit models for the perineurium. In their discussion, they note that two of the circuits are more likely candidates, given the cellular structure of the perineurium. Calculating the total sheet resistance at 10 kHz for the two circuits yielded 0.0176 Ω-m^2 and 0.0159 Ω-m^2, with a mean of **0.0168 Ω-m^2**. This value is close to the value of 0.0111 Ω-m^2 used by Frieswijk 1998 (Frieswijk et al., 1998) in which they also estimated the sheet resistance at 10 kHz from Weerasuriya's data. The sheet resistance at 10 kHz is relevant in considering the frequency spectrum of short stimulation pulses and for typical kilohertz frequencies used for neural block (Kilgore and Bhadra, 2014).

ii. **Weerasuriya, 10 kHz, 37°C**: Combining cases ii and iii from above, we estimated the perineurium sheet resistance at 10 kHz and 37°C as **0.0088 Ω-m^2**:

$$R_{S,37oC} = \left[\left(\frac{1}{R_{S,21oC}}\right) * Q_{10}^{\frac{\Delta T\, in\, degC}{10}}\right]^{-1} = \left[\left(\frac{1}{0.0168\,\Omega \cdot \mathrm{m}^2}\right) * (1.5)^{\frac{37-21}{10}}\right]^{-1} = 0.0088\,\Omega \cdot \mathrm{m}^2$$

i. **Common value in literature**: Many publications used a sheet resistance of **0.0149 Ω-m^2** (Supplement A) by modeling the perineurium with a resistivity of ~300 Ω-m and a thickness of 50 μm, which translates to a constant sheet resistance. However, it is unclear how this resistivity was obtained from the Weerasuriya impedance measurements, e.g., footnote in Goodall et al. 1995 (Goodall et al., 1995).

We implemented these five values for the perineurium sheet resistance in different ways (Methods A, B, C, and D in Table 2). For Methods A and B, we used COMSOL's contact impedance boundary condition to model the perineurium. In **Method A**, we used the *same sheet resistance across fascicle diameters*, equivalent to modeling the perineurium with constant resistivity and thickness (examples in Supplement A where the perineurium

[1] Note that the text in Weerasuriya 1984 (abstract and main body) reports 0.0478 Ω-m^2 as the DC value of perineurium specific resistance, but their four equivalent circuits all produce 0.0439 Ω-m^2 at 0 Hz.

thickness is a constant). In **Method B**, we used the *same resistivity across fascicle diameters*. Grinberg found that the perineurial thickness is ~3% of the fascicle diameter (Grinberg et al., 2008). For the frog sciatic nerves used to measure the perineurial impedance, Weerasuriya reported that the fascicle (i.e. nerve) diameters ranged from 0.65 to 0.8 mm (mean = 0.725 mm; consistent with other frog sciatic nerve diameters in literature (Rao, 1978)). Thus, we can estimate the perineurial thickness of Weerasuriya's frog sciatic nerve samples (3% * 0.725 mm = 21.75 μm). This agrees with our histology on frog sciatic nerve from which we measured perineurial thickness of ~25 μm (data not shown). Then each of the five sheet resistance values outlined above were converted to resistivity (Table 2, column D). Finally, to model the perineurium with constant resistivity as a contact impedance boundary condition, we converted the resistivity values to sheet resistance values by multiplying the resistivity by the perineurial thickness for each fascicle size (thk_{peri} = 3%*d_{fasc}).

In **Methods C and D**, we again used constant sheet resistance (as in Method A) and constant resistivity (as in Method B), respectively, but modeled the perineurium as a thin meshed layer with a thickness set to 3% of the fascicle diameter. Thus, the resistivity values in C and D are equal to A and B divided by the perineurium thickness.

We evaluated the effects of perineurium representation and resistivity using a simplified model with a single fascicle in the centre of the nerve and a realistic nerve model with 10 fascicles. We evaluated two radii (0.1 and 0.3 mm) for the fascicle centred in each nerve model and four axon locations within each fascicle: centred (x_0,y_0) and three positions around the fascicle periphery ((x_0,y_0±0.75*r_{fasc}) and (x_0+0.75*r_{fasc},y_0)). We evaluated two electrode designs (monopolar partial cuff and bipolar circumneural cuff) and calculated thresholds for 2 and 10 μm diameter axons using a 0.1 ms cathodic pulse. For the bipolar circumneural cuff with the simplified and multifascicular nerve models, we also calculated block thresholds for the 2 μm axon with 5, 10, and 20 kHz sinusoids. For the block thresholds, we evaluated perineurial sheet resistance and resistivity values at 0 Hz (DC) and at the frequency corresponding to the stimulus waveform, each at room and body temperature (Table 2).

2.4. Modeling the Endoneurium

Bulk endoneurium is uniaxially anisotropic, with larger transverse resistivity than longitudinal resistivity. The resistivity measured *in vivo* for the cat dorsal columns was 1.75 and 12 Ω-m in the longitudinal and transverse directions, respectively (Ranck and Bement, 1965), and these values are widely used in modeling peripheral nerve and spinal cord stimulation (Howell et al., 2015; Lempka et al., 2015; Pelot et al., 2017; Schiefer et al., 2012). The longitudinal resistivity estimate is in good agreement with the measurement for *ex vivo* toad sciatic nerve of 2 Ω-m, although the toad experiments were performed at room temperature (Tasaki, 1955). The transverse resistivity for the toad nerve was reported as 100 Ω-m (Tasaki, 1955), but this included perineurium and epineurium; the transverse resistivity was recalculated as 5.6 Ω-m using estimates of the histological composition of the nerve and for resistivity of endoneurial fluid (0.8 Ω-m for amphibian Ringer's solution) (Altman and Plonsey, 1989). The longitudinal and transverse resistivities of cat internal capsule were

found to be 0.85 and 8 Ω-m, respectively (Geddes and Baker, 1967a; Nicholson, 1965). While the dorsal column and internal capsule measurements are in good agreement, these are bundles of mostly myelinated axons, whereas many nerves of interest (e.g., vagus) contain primarily unmyelinated axons (Agostoni et al., 1957; Mei et al., 1980; Prechtl and Powley, 1990).

We used three approaches to determine the most appropriate representation of the endoneurium. First, we used an analytical approach to estimate the bulk transverse endoneurial resistivity. Second, we used a numerical approach to estimate the bulk transverse resistivity where we used two 2D models of a fascicle. In Model 1, we modeled the cross section of a fascicle with axons and connective tissue. In Model 2, we modeled the fascicle as a homogeneous circle and swept the bulk transverse endoneurial resistivity to match the extracellular potentials of Model 1. Third, we quantified the effects of changing the bulk endoneurial resistivity on axon activation thresholds.

2.4.1. Analytical Expression to Estimate Bulk Transverse Endoneurial Resistivity—The analytical expression for the bulk transverse resistivity of a random, uniform distribution of parallel cylinders in a medium is given by:

$$\frac{1-\frac{\rho_{medium}}{\rho_{bulk}}}{1+\frac{\rho_{medium}}{\rho_{bulk}}} = F\left[\frac{1-\frac{\rho_{medium}}{\rho_{cyl}+\frac{Z_m}{a}}}{1+\frac{\rho_{medium}}{\rho_{cyl}+\frac{Z_m}{a}}}\right] \quad (2)$$

where ρ_{bulk} = bulk transverse resistivity (Ω-m), F = volume fraction of cylinders (unitless), ρ_{medium} = medium resistivity (Ω-m), ρ_{cyl} = resistivity inside the cylinders (Ω-m), a = cylinder radius, and Z_m = specific membrane impedance (Ω-m^2) (Cole and Curtis, 1936; Curtis and Cole, 1938). The derivation of this equation required several assumptions. First, the cylinders were assumed to be homogeneous conductors ensheathed with thin[2], high impedance[3] membranes (Cole and Curtis, 1936; Curtis and Cole, 1938). Second, the medium surrounding the cylinders was assumed to be a homogeneous conductor (Cole and Curtis, 1936). Third, while we could neglect longitudinal current flow if we assumed that the electrodes were long and parallel to the longitudinal axes of the cylinders (Cole and Curtis, 1936), the first two assumptions instead allow decoupling of the longitudinal and transverse current flows (Cranford et al., 2012; Meffin et al., 2014, 2012); thus, we only considered the transverse dimension of the problem, and the volume fraction of the cylinders (F) could be equivalently considered as a cross-sectional area fraction (AAF; axonal area fraction). Fourth, the effective electric field for each cylinder was assumed to be uniform (Cole et al., 1969; Meffin et al., 2014). Finally, the volume fraction of the cylinders was initially assumed to be less than 0.5 in the analytical derivation, but the equation was validated experimentally to volume fractions greater than 0.9 (Cole et al., 1969).

[2] "Thin": ((radius of cylinder to inner surface of membrane)/(radius of cylinder to outer surface of membrane))^2 ~ 1
[3] "High impedance": $\rho_{membrane} \gg \rho_{intra\text{-}cylinder}$; $\varepsilon_{membrane} \ll \varepsilon_{intra\text{-}cylinder}$

In Equ. 2, the membrane impedance, Z_m, incorporates a specific membrane resistance (R_m) and a polarization impedance: $Z_3 = R_m + \overline{z_3}(j\omega)^{-\alpha}$, for which ω is the angular frequency of the applied current and α is related to the phase angle, $\phi = \alpha\pi/2$ (Cole and Curtis, 1936). Because we applied direct current to our model and operated under the quasi-static assumption ($\omega = 0$), Z_3 reduced to R_m. We thus simplified Equ. (2) and solved for ρ_{bulk}:

$$\rho_{endo-bulk-transverse} = \rho_{endo-micro} * \frac{1+A}{1-A} \text{ where } A = AAF * \frac{1 - \frac{\rho_{endo-micro}}{\rho_a + \frac{R_m}{d_{axon}/2}}}{1 + \frac{\rho_{endo-micro}}{\rho_a + \frac{Rm}{d_{axon}/2}}} \quad (3)$$

where $\rho_{bulk} = \rho_{endo\_bulk\_transverse}$, $F = AAF$, $\rho_{medium} = \rho_{endo\_micro}$, $\rho_{cyl} = \rho_a$, $a = d_{axon}/2$, and $Z_m = R_m$.

We compared $\rho_{endo\text{-}bulk\text{-}transverse}$ calculated using the analytical approach (Equ. 3) across a range of parameter values (Table 3) to $\rho_{endo\text{-}bulk\text{-}transverse}$ estimated from a numerical model (Model 2, see Section 2.4.2).

2.4.2. Two-Dimensional Finite Element Models to Estimate Bulk Transverse Endoneurial Resistivity—We implemented two 2D FEMs in COMSOL to estimate the bulk transverse endoneurial resistivity (Figure 3). Model 1 (gold standard) represented a cross section of a cylindrical fascicle containing unmyelinated axons (free triangular quadratic isoparametric elements; 1,289,407 elements with default model parameters listed in Table 3), and Model 2 (bulk approximation) represented a cross section of a homogenized fascicle without explicitly-modeled axons (25,970 elements with default parameters). For Model 1, we used geometrical and electrical parameter values based on the anatomy and microscopic electrical properties of the mammalian abdominal vagus nerve (Table 3). We randomly placed the axons using disk point picking method to ensure that the axons were uniformly distributed within the fascicle, and we imposed a minimum distance of $d_{axon}/10$ from the boundary of the fascicle to each axon and between neighbouring axons. We modeled the axonal membranes using COMSOL's contact impedance boundary condition (verified in Supplement B).

For each of the two models, we quantified the distribution of potentials generated using two different electrode configurations. First, we applied 1000 A/m^2 to the top right quarter of the fascicle circumference and grounded the bottom left quarter (Figure 3 and Figure 5(a)). The remaining two quarters of the fascicle circumference were insulated. Second, to ensure that our estimates of the bulk endoneurial resistivity were independent of electrode configuration, we used two small 1000 A/m^2 contacts and one ground to create a less uniform field distribution (Figure 5(b)).

We determined the electric potential at thousands of points within the fascicle (12,939 points with default parameters) using a grid with 0.5 μm spacing, excluding points inside an axon or within $d_{axon}/10$ from a boundary. We varied $\rho_{endo\text{-}bulk\text{-}transverse}$ of Model 2 in 0.01 Ω-m

increments to find the value at which the residual sum of squares (RSS) was minimized, comparing the sampled intrafascicular potentials of Model 1 (V_{endo1}) and Model 2 (V_{endo2}):

$$RSS = \Sigma(V_{endo2} - V_{endo1})^2 \quad (4)$$

We conducted sensitivity analyses of the three electrical parameters of Model 1 (ρ_a, R_m, and $\rho_{endo\text{-}micro}$) and of the fascicle and axon diameters across their physiological ranges (Table 3). We also examined the effects of the spatial arrangement of axons. We initially placed the axons randomly using disk point picking, but this limited the maximum achievable axonal area fraction (AAF) to 0.435. To achieve a higher AAF, we placed axons in a grid formation with a reduced minimum distance between boundaries. To vary the AAF, we randomly removed axons from the grid, producing quasi-structured placements. We analysed the effects of AAF, minimum distance between object boundaries, and random versus quasi-structured axon placements.

2.4.3. Effects of Bulk Endoneurial Resistivity on Threshold—We quantified activation thresholds while varying the values for the longitudinal and transverse endoneurial resistivity. For the simplified nerve model with two fascicles, we evaluated two electrode designs, two fascicle radii (r_{fasc} = 0.1 and 0.3 mm), two fascicle locations, and four axon locations within each fascicle (Figure 2 and Supplement F). For the realistic nerve model, we evaluated 10 fascicle diameter-location pairs (one for each fascicle) with two fascicle radii for the centre fascicle (r_{fasc} = 0.1 or 0.3 mm), four axon locations within each fascicle, and two axon diameters (2 and 10 μm) (Figure 2 and Supplement F).

3. Results

Using computational models, we quantified the effects of different representations of the perineurium and of the bulk resistivity of the anisotropic endoneurium on thresholds to activate and block model axons.

3.1. Effects of Representation of the Perineurium on Thresholds

We compared activation and block thresholds (Figure 4 and Supplement D) using different estimates for the properties of the perineurium (Table 2) in a simplified nerve model with a single fascicle and in a realistic nerve model with 10 fascicles. We evaluated two fascicle diameters for the centre fascicle, four axon locations within each fascicle, two electrode geometries, and two axon diameters. Electrode geometry, axon diameter, fascicle diameter, and perineurium resistivity had substantial effects on activation and block thresholds, while perineurium representation (thin meshed layer vs. boundary condition) and axon location within a fascicle had little effect on threshold.

The bipolar circumneural cuff resulted in higher thresholds than the monopolar partial cuff (Supplement D, Figure 10(a) vs. (b)); the presence of neighbouring axons in the multifascicular model increased thresholds for axons in the centre fascicle (Supplement D, Figure 10(b) and (c) insets vs. red data in (d) and (e)); and the 10 μm axons had lower thresholds than the 2 μm axons (Supplement D, Figure 10(b) vs. (c) and (d) vs. (e)). The

effects of perineurium representation and resistivity on activation thresholds were qualitatively similar across electrode geometries, single vs. multifascicular nerve models, and fibre diameters.

Lower perineurium resistance (i) to (iv), at warmer temperatures and higher frequencies (Table 2), resulted in lower thresholds. Thresholds increased approximately linearly with increasing resistivity (Figure 4(b); Supplement D, Figure 10(b) inset, Figure 10(c) inset, Figure 10(d), and Figure 10(e)). Specifically, activation thresholds increased with higher perineurium resistivity (~400 vs. 2200 Ω-m), with one exception, yielding larger increases for smaller diameter axons and for axons in larger fascicles: ~15 to 115% increase in the single fascicle model (~30 to 115% for 2 μm axons; ~15 to 70% for 10 μm axons); up to ~130% for 2 μm axons and ~75% for 10 μm axons in the multifascicular model across four axons in each of the 10 fascicles. In the case of 10 μm fibres in the smallest fascicle of the multifascicular model (grey in Supplement D, Figure 10(d) and (e)), thresholds decreased slightly (<3%) with increased perineurium resistivity, likely due to increased current deflection around neighbouring fascicles.

Across all representations of the perineurium, axons in the centre fascicle had higher activation and block thresholds when the fascicle radius was larger, and the effect of fascicle size on thresholds was comparable to the changes in threshold due to different representations of the perineurium. When the radius of the centre fascicle was reduced from 0.3 to 0.1 mm, thresholds for axons in that fascicle increased with larger fascicle radius, yielding a larger increase with higher perineurium resistivity: ~65 to 175% increase for 2 μm axons in the single fascicle model; ~55 to 180% for 2 μm axons and ~30 to 100% for 10 μm axons in the multifascicular model.

Thresholds were higher with the representations assuming constant perineurial sheet resistance (Figure 4(a), Methods A and C) than with representations assuming constant perineurial resistivity (Figure 4(a), Methods B and D) as the former had a more resistive perineurium and diverted more current around the fascicle. Thresholds with the perineurium represented using the contact impedance boundary condition (Methods A and B) were quite similar to the thresholds with the perineurium explicitly meshed (Methods C and D) with different electrode designs and fibre diameters.

Lastly, axons at different locations within a given fascicle had similar thresholds (Supplement D) due to the high perineurial resistivity causing the potentials to be approximately uniform across the fascicle cross section (Figure 2). As expected, the thresholds were higher for the axon furthest from the partial cuff and the differences in thresholds were greater for axons in a larger fascicle than in a smaller fascicle.

In addition to activation thresholds for a 0.1 ms cathodic pulse, we determined thresholds to block action potential conduction in a single 2 μm axon centred in the fascicle with 5, 10, and 20 kHz sinusoidal signals (Figure 4(c) to (e)) using the contact impedance boundary condition. As observed for activation, axons in larger fascicles had higher block thresholds; for a given KHF and fascicle size, block thresholds were higher with greater perineurium resistivity; and block thresholds were higher for an axon centred in the middle fascicle in the

multifascicular model than the single fascicle model. Lower frequency KHF sinusoidal signals have lower block thresholds (Bhadra et al., 2006; Pelot et al., 2017), and this was observed using constant sheet resistance (Method A) or constant resistivity (Method B) across fascicle sizes for perineurium resistance estimates at DC at 21°C (i) or 37°C (ii). The higher thresholds with higher KHF were maintained when using frequency-appropriate perineurium resistance in all cases but one. The frequency-dependent perineurium sheet resistance or resistivity had lower values for higher frequencies and thus reduced the threshold differences across KHF inputs; in the case of the large fascicle at 21°C in the single fascicle model, we observed lower thresholds with higher KHF.

3.2. Modeling the Endoneurium

3.2.1. Analytical and Numerical Estimates of Bulk Endoneurial Resistivity—

We used both analytical and numerical approaches to estimate the value of the bulk endoneurial resistivity for a bundle of unmyelinated axons. The analytical expression (Equ. 3) resulted in $\rho_{endo\text{-}bulk\text{-}transverse}$ = 1.65 Ω-m for default parameter values (Table 3). With our numerical approach, we optimized the value of $\rho_{endo\text{-}bulk\text{-}transverse}$ in a homogeneous model of a fascicle (Model 2) to minimize the residual sum of squares of sampled extracellular potentials as compared to Model 1 with explicitly represented unmyelinated axons. Using the default parameter values (Table 3), we estimated $\rho_{endo\text{-}bulk\text{-}transverse}$ = 1.73 Ω-m with the model yielding less than 5% error as compared to the analytical solution.

We compared $\rho_{endo\text{-}bulk\text{-}transverse}$ for two different electrode configurations that yielded significantly different potential distributions (Figure 5(a) and (b)), and we obtained 1.73 and 1.76 Ω-m, respectively, with the numerical approach. Further, the $\rho_{endo\text{-}bulk\text{-}transverse}$ values extracted from the two electrode configurations differed by less than 2% across different $\rho_{endo\text{-}micro}$ and AAF values (AAF = 42.5% with $\rho_{endo\text{-}micro}$ = 0.65, 1.3, 2 and AAF = 22.5% with $\rho_{endo\text{-}micro}$ = 0.65), suggesting that $\rho_{endo\text{-}bulk\text{-}transverse}$ is independent of electrode configuration.

We determined the effects of varying the electrical parameters (ρ_a, R_m, $\rho_{endo\text{-}micro}$) and the geometrical parameters (d_{fasc}, axon placement, d_{axon}) on the $\rho_{endo\text{-}bulk\text{-}transverse}$ estimate across physiologically relevant ranges (Table 3). The numerical and analytical estimates (1.73 Ω-m and 1.65 Ω-m, respectively) were each constant to within 0.01 Ω-m over the entire range of ρ_a and R_m values. Inspection of the current density indicated that there was negligible current entering the axons, thus explaining the lack of sensitivity to these electrical parameters, contingent simply upon R_m rendering the axonal membrane highly resistive (Supplement E).

Both the numerical and analytical estimates of $\rho_{endo\text{-}bulk\text{-}transverse}$ increased linearly with $\rho_{endo\text{-}micro}$ (Figure 6(a)) and varied minimally with fascicle diameter (Figure 6(b)). As for the effects of axon placement – which does not figure into the analytical equation – and of axon diameter, we obtained $\rho_{endo\text{-}bulk\text{-}transverse}$ = {1.73, 1.73, 1.74} Ω-m for three different random placements of 1 μm axons (n = 4796), while two different random placements of 2 μm axons (n = 1199) yielded $\rho_{endo\text{-}bulk\text{-}transverse}$ = {1.71, 1.73} Ω-m. These results demonstrate that $\rho_{endo\text{-}bulk\text{-}transverse}$ is insensitive to the specific random placement of axons and to d_{axon} within physiological range. We did not evaluate 0.5 μm axons due to the

computational requirements to model over 19000 axons, as required to cover 43.5% of the cross-sectional area of a 105 μm fascicle. The analytical expression predicted 1.65 Ω-m for all three d_{axon} values.

We also examined the effects of varying the axonal area fraction (AAF) and axon placement on the $\rho_{endo\text{-}bulk\text{-}transverse}$ estimates. For randomly placed axons, both the model and analytical expression predicted increased $\rho_{endo\text{-}bulk\text{-}transverse}$ with increasing AAF (Figure 6(c) and (d)), which was expected since an increasing proportion of the fascicle's cross-sectional area was comprised of effectively insulated circles (Supplement E). With quasi-structured axonal placement and reduced minimum inter-axonal distance, $\rho_{endo\text{-}bulk\text{-}transverse}$ still increased with AAF, but we observed larger deviations from the analytical solution, particularly as the AAF increased and as the minimum distance between axons decreased (Figure 6(c) and (d)).

Figure 7 reveals a likely explanation for the increasing discrepancy between $\rho_{endo\text{-}bulk\text{-}transverse}$ estimates with the numerical and analytical approaches at higher AAF values and smaller inter-axonal distances. As we decreased the minimum spacing, the potential distribution became less smooth and the electric field became less uniform, while the analytical expression assumes a uniform electric field. These non-uniformities arise from current deflection around clusters of closely-packed axons. We compared the potentials and electric fields from random (Figure 5(a) and (c)), structured (Figure 7(i) and (j)), and quasi-structured placements (Figure 7(a) to (h)). While the random axon placement yielded a relatively uniform electric field, the structured placement forced the current to flow around the outer rim of the fascicle, and the quasi-structured placement imposed preferred current paths. Thus, the latter two cases violated the assumption of uniform electric field used in the derivation of Equ. 3. These issues are reduced at lower AAF values and at larger minimum inter-axon distances where the axons are more loosely packed, resulting in relatively uniform current flow across the fascicle.

3.2.2. Effects of Bulk Endoneurial Resistivity on Activation Thresholds—We quantified the sensitivity of activation thresholds (Figure 8 and Supplement F) to changes in the anisotropic bulk endoneurial resistivity in two models of a nerve (simplified nerve model with two small fascicles (r_{fasc} = 0.1 mm) or two large fascicles (r_{fasc} = 0.3 mm) and realistic nerve model with 10 fascicles, changing the radius of the centre fascicle) and two models of a cuff electrode (monopolar partial cuff and bipolar circumneural cuff electrodes) (Figure 2). Changing $\rho_{endo\text{-}transverse}$ from 1.75 to 25 Ω-m (default = 12 Ω-m) caused minimal changes in thresholds. Conversely, changing $\rho_{endo\text{-}longitudinal}$ from 0.75 to 3.5 Ω-m (default = 1.75 Ω-m) caused significant changes in threshold. Specifically, examining the thresholds across four axons in each of 10 fascicles in the multifascicular model (Supplement F), activation thresholds increased by ~35 to 250% for lower longitudinal endoneurium resistivity (3.5 vs. 0.75 Ω-m), with larger increases for smaller diameter axons and for axons in larger fascicles. In addition, changing both $\rho_{endo\text{-}longitudinal}$ and $\rho_{endo\text{-}transverse}$ with constant $\rho_{endo\text{-}ratio}$ = $\rho_{endo\text{-}transverse}/\rho_{endo\text{-}longitudinal}$ = 12 Ω-m/1.75 Ω-m = 6.9 (varying $\rho_{endo\text{-}longitudinal}$ from 0.875 to 3.5 Ω-m and $\rho_{endo\text{-}transverse}$ from 6 to 24 Ω-m) also caused substantial changes in threshold. Thus, thresholds were highly sensitive to $\rho_{endo\text{-}longitudinal}$, but comparably insensitive to $\rho_{endo\text{-}transverse}$. As observed generally, for a given fascicle position, axons in a

smaller fascicle had lower thresholds than in a larger fascicle, and axon position within a fascicle did not substantially affect threshold (Supplement F).

4. Discussion

We studied the sensitivity of activation thresholds to the electrical properties of the perineurium and endoneurium of compound peripheral nerves. There are different approaches to represent these tissues within computational models, and we clarified the impact of these choices. We demonstrated substantial differences in activation and block thresholds when accurately modeling the highly resistive perineurium using appropriate temperature and frequency, while maintaining constant resistivity across different fascicles with perineurial thicknesses proportional to fascicle diameter. We estimated the bulk transverse endoneurial resistivity using numerical and analytical techniques, revealing a value approximately an order of magnitude lower than typically used, although we also found that activation thresholds were only weakly sensitive to the transverse resistivity and much more sensitive to the longitudinal endoneurial resistivity. Given growing interest in peripheral nerve stimulation, a critical examination of parameter values used in computational modeling studies is fundamental to effective development of neural stimulation therapies.

4.1. Simplified Versus Multifascicular Nerve Models

We found comparable changes in thresholds across perineurial and endoneurial resistivities between the simplified and multifascicular nerve models, although the latter yielded higher thresholds due to the addition of resistive elements (i.e., fascicles with perineurial sheaths) between the target fascicle and the electrode. Axons with smaller diameters and/or axons placed in larger fascicles exhibited larger changes in threshold with changes in resistivities. Further, the effect of fascicle size was greater when using resistivities that produced higher thresholds, i.e. higher ρ_{peri} or lower $\rho_{endo\text{-}longitudinal}$.

4.2. Modeling the Perineurium

We compared activation thresholds with different representations of the perineurium and observed lower activation and block thresholds when using lower perineurial resistivities. The most accurate estimate with currently available data involved computing the resistivity from the perineurial sheet resistance measured from frog sciatic nerve, assuming that the perineurium thickness was 3% of the fascicle diameter, at the primary frequency peak of the stimulation waveform, averaging equivalent circuits A and B in Weerasuriya, and then scaling the result to 37°C using a Q_{10} factor. The perineurium can then be modeled with the resulting resistivity either as a thin meshed layer, 3% of the fascicle diameter, or with COMSOL's contact impedance boundary condition, which reduces computational demands while producing comparable thresholds. While the perineurium is often modeled using a constant resistivity and thickness for all fascicle diameters (Supplement A), the perineurial thickness varies with fascicle diameter (Grinberg et al., 2008; Williams et al., 2000); therefore, it should instead be modeled with a constant resistivity across fascicle diameters, either implemented with a boundary condition with fascicle diameter-dependent sheet resistance or as a thin meshed layer with fascicle diameter-dependent thickness.

4.3. Modeling the Endoneurium

We estimated the bulk transverse resistivity of an unmyelinated fibre bundle and quantified the effects of endoneurial resistivity on activation thresholds. The default parameters representing the abdominal vagus nerve (Table 3) yielded $\rho_{endo\text{-}bulk\text{-}transverse}$ of ~1.75 Ω-m both numerically and analytically, and this estimate was highly sensitive to AAF. We found strong agreement between the numerical and analytical estimates of $\rho_{endo\text{-}bulk\text{-}transverse}$, except for cases with high AAF and small minimum inter-axonal distances (Figure 6). Specifically, the numerical estimate for $\rho_{endo\text{-}bulk\text{-}transverse}$ was insensitive to different random arrangements of axons, but deviated from the analytical estimate when using quasi-structured arrangements. As seen in Figure 5(c) and (d), the electric field was relatively uniform across a fascicle with randomly placed axons. Different random arrangements of axons and different electrode configurations produced similarly uniform electric fields, thus producing consistent $\rho_{endo\text{-}bulk\text{-}transverse}$ estimates. However, the axon clusters in the quasi-structured axon placements distorted the electric field, and this distortion increased as the space between axons decreased (Figure 7). The analytical expression assumes a uniform electric field, and spatial arrangements of axons that resulted in a uniform electric field (i.e. random arrangements and low axon densities) produced a $\rho_{endo\text{-}bulk\text{-}transverse}$ similar to that of the analytical expression, while arrangements that distorted the electric field (quasi-structured) did not.

Our numerical simulations of a bundle of unmyelinated axons revealed that negligible current entered the intracellular space from transverse current flow, despite the lack of myelin, due to the high specific resistance of the axonal membrane and the lower resistance of the extracellular pathways. $\rho_{endo\text{-}bulk\text{-}transverse}$ was largely insensitive to intracellular resistivity (ρ_a), specific membrane resistance (R_m), axon diameter (d_{axon}), and fascicle diameter (d_{fasc}). These results were expected from Equ. 3 given that fascicle diameter does not figure in the equation, and by considering the relevant values of the other three parameters. Specifically, over the range of physiological axon diameters, the term $\frac{R_m}{d_{axon}/2}$ is much larger than ρ_a, yielding $\frac{\rho_{endo-micro}}{\rho_a + \frac{R_m}{d_{axon}/2}} \approx \frac{\rho_{endo-micro}}{\frac{R_m}{d_{axon}/2}}$. Since this term is much less than one, the expression for A reduces to $A = AAF * 1$. Consequently, Equ. 3 reduces to Equ. 4, as used in (Altman and Plonsey, 1989) for the bulk resistivity of non-conducting cylinders:

$$\rho_{endo-bulk-transverse} = \rho_{endo-micro} * \frac{1 + AAF}{1 - AAF} \quad (4)$$

Thus, $\rho_{endo\text{-}bulk\text{-}transverse}$ should be affected only by changes in AAF or $\rho_{endo\text{-}micro}$, as was observed in Figure 6. Further, this indicates that the analytical formulation applies equally well to unmyelinated and myelinated axons at steady-state; the modeled unmyelinated axons, like myelinated fibres, are effectively insulated cylinders, and transverse current flow is predominantly carried by the interstitial fluid in both cases. Further, the AAF may differ between fibre bundles (e.g., different nerves, different distributions of myelinated vs. unmyelinated axons), and a higher AAF would increase the current redistribution between the intracellular and extracellular domains (Roth and Gielen, 1987). We can compare the

analytical estimate to experimental measurements from myelinated axons. The transverse resistivity of cat dorsal columns was measured as 12.11 Ω-m, and the estimated interstitial volume fraction was 13%, which agrees with other estimates of ~10–12% for the rabbit spinal cord (Bourne, 1972; Davson et al., 1962; Ranck and Bement, 1965). Assuming AAF = 0.90, Equ. 3 predicts $\rho_{endo\text{-}bulk\text{-}transverse}$ = 12.35 Ω-m, which is only 2% larger than the Ranck and BeMent measurement. If AAF is indeed close to 1, then the analytical estimate of $\rho_{endo\text{-}bulk\text{-}transverse}$ can be further simplified from Equ. 4; defining $b = d_{axon} + dist_{min}$, if $AAF \rightarrow 1$, then $dist_{min} \ll d_{axon}$, $dist_{min} \ll b$, and AAF can be simplified:

$$AAF \cong \frac{\pi * d_{axon}^2}{\pi * b^2} = \frac{(b - dist_{min})^2}{b^2} = \left(\frac{b - dist_{min}}{b}\right)^2 = \left(1 - \frac{dist_{min}}{b}\right)^2 = 1 - 2 * \frac{dist_{min}}{b} + \left(\frac{dist_{min}}{b}\right)^2 \cong 1 - 2 * \frac{dist_{min}}{b} \quad (5)$$

Equ. 5 can be substituted into Equ. 4, reproducing the expression for the bulk transverse endoneurial resistivity in (Meffin et al., 2014; Tahayori et al., 2014):

$$\rho_{endo-bulk-transverse} = \rho_{endo-micro} * \frac{1 + \left(1 - \frac{2dist_{min}}{b}\right)}{1 - \left(1 - \frac{2dist_{min}}{b}\right)} = \rho_{endo-micro} * \frac{b - dist_{min}}{dist_{min}} \cong \rho_{endo-micro} * \frac{b}{dist_{min}} \quad (6)$$

Using the nominal values from (Tahayori et al., 2014), $\rho_{endo\text{-}micro}$ = 0.7 Ω-m, b = 0.5 μm, and $dist_{min}$ = 0.05 μm, yields $\rho_{endo\text{-}bulk\text{-}transverse}$ = 7 Ω-m, which is the same order of magnitude as our estimates.

Regardless of these findings with respect to $\rho_{endo\text{-}bulk\text{-}transverse}$, activation thresholds were approximately constant when varying the transverse endoneurial resistivity (Figure 8) since the perineurium has a more important role in shaping the transverse electric field. However, for larger fascicles or monofascicular nerves, the value of $\rho_{endo\text{-}bulk\text{-}transverse}$ affects thresholds and thresholds may vary with intrafascicular axon location. Conversely, thresholds were sensitive to the longitudinal endoneurial resistivity due to the fact that polarization of the transmembrane potential is driven by the second difference of the extracellular potentials along the axon. With higher $\rho_{endo\text{-}longitudinal}$, the second difference of the transmembrane potentials had a larger magnitude (i.e. more rapid spatial change in potentials), resulting in a lower stimulation threshold.

In the case of longitudinal current flow, there is current redistribution between the intracellular and extracellular spaces over the length constant of the axon (Altman and Plonsey, 1989). For tightly-packed axons at steady-state in a far-field model (such as cuff around a compound nerve), the longitudinal bulk endoneurial resistivity is approximately equal to the intracellular resistivity, i.e. ~0.7 Ω-m (Tahayori et al., 2014). Alternatively, the intracellular and extracellular (i.e. micro-endoneurial) spaces can be considered as parallel resistors, and the resistivity of the equivalent total resistance can be calculated:

$$\rho_{endo\_longitudinal} = (A_{axon} + A_{endo}) * \left(\frac{\rho_a * \rho_{endo-micro}}{\rho_a * A_{endo} + \rho_{endo-micro} * A_{axon}} \right) \quad (7)$$

where A_{axon} is the total cross-sectional area covered by all axons and A_{endo} is the cross-sectional area covered by the endoneurial connective tissue in the extracellular space. The intracellular and extracellular spaces have approximately equal resistivities (nominal values of 0.7 and 0.65 Ω-m, respectively (Table 1)). These estimates of $\rho_{endo\text{-}longitudinal}$ compare well to the standard value in literature of 1.75 Ω-m (Ranck and Bement, 1965), considering additional resistance presented by the membrane during current redistribution.

Overall, these estimates support the prior literature of *in vivo* measurements and modeling parameters where the transverse resistivity of a bundle of axons is approximately 10 times that of the longitudinal resistivity. However, we did not model any additional elements known to be present in the interstitial space, such as neuroglia and microvasculature (Topp and Boyd, 2006; Zhang and Sejnowski, 2000). While it is unknown to what degree these elements carry transverse current, they at least restrict the volume of interstitial fluid (Ranck and Bement, 1965). Further, we did not account for frequency-dependent tissue impedances, including the axonal membrane capacitance which would reduce the axonal membrane impedance at higher frequencies. Despite these limitations, our study provides much needed insight into the bulk electrical properties of unmyelinated fibre bundles and into the sensitivity of thresholds to endoneurial resistivity, which will prove to be invaluable for modeling novel neurostimulation devices for unmyelinated nerves.

5. Conclusions

We performed a systematic investigation of the effects of values and methods for modeling the perineurium and endoneurium on activation and block thresholds, which provides critical guidance on electrical parameter values for future modeling studies and may help address discrepancies between modeling and experimental data. The temperature and frequency should be considered for the perineurium resistivity, and it can be modeled as a sheet resistance boundary condition calculated using an appropriate perineurial thickness. The longitudinal endoneurial resistivity has a greater impact on thresholds than the transverse resistivity, and the latter is ~10x larger. With growing interest in peripheral nerve stimulation to treat diseases, it is important to leverage the capacity of computational modeling to explore broad ranges of geometrical and electrical parameter values for the nerve and electrode while being mindful of the accuracy and underlying assumptions of the chosen values.

Supplementary Material

Refer to Web version on PubMed Central for supplementary material.

Acknowledgements

The authors wish to acknowledge Dr. Boshuo Wang for his insights into the numerical and analytical estimates of the bulk endoneurial resistivity and Dr. Craig Henriquez for his review of the manuscript.

Research supported by NIH OT2 OD025340, Fulbright Canada (15122811), the Natural Sciences and Engineering Research Council of Canada (PGS M-425353-2012 and PGS D3-437918-2013), the Triangle Community Foundation (Gertrude B. Elion Mentored Medical Student Research Award), and Duke University (Medical Scientist Training Program [NIH T32 GM007171], James B. Duke Fellowship, Robert Plonsey Fellowship, and Pratt School of Engineering Faculty Discretionary Fund).

References

Agostini E, 1957 Functional and histological studies of the vagus nerve and its branches to the heart, lungs and abdominal viscera in the cat. J Physiol 135, 182–205. [PubMed: 13398974]

Agostoni E, Chinnock JE, De Daly MB, Murray JG, 1957 Functional and histological studies of the vagus nerve and its branches to the heart, lungs and abdominal viscera in the cat. J. Physiol. (Lond.) 135, 182–205. [PubMed: 13398974]

Altman KW, Plonsey R, 1989 Analysis of the longitudinal and radial resistivity measurements of the nerve trunk. Ann Biomed Eng 17, 313–324. [PubMed: 2774310]

Barrett J, Crill W, 1974 Specific membrane properties of cat motoneurones. J Physiol 239, 301–24. [PubMed: 4137933]

Bhadra N, Peckham PH, 1997 Peripheral nerve stimulation for restoration of motor function. J Clin Neurophysiol 14, 378–393. [PubMed: 9415385]

Bhadra Narendra, Bhadra Niloy, Kilgore K, Gustafson KJ, 2006 High frequency electrical conduction block of the pudendal nerve. J. Neural Eng 3, 180–187. 10.1088/1741-2560/3/2/012 [PubMed: 16705274]

Birmingham K, Gradinaru V, Anikeeva P, Grill WM, Pikov V, McLaughlin B, Pasricha P, Weber D, Ludwig K, Famm K, 2014 Bioelectronic medicines: a research roadmap. Nat. Rev. Drug Discov 13, 399–400. 10.1038/nrd4351 [PubMed: 24875080]

Bossetti CA, Birdno MJ, Grill WM, 2008 Analysis of the quasi-static approximation for calculating potentials generated by neural stimulation. J. Neural Eng 5, 44–53. 10.1088/1741-2560/5/1/005 [PubMed: 18310810]

Bourne G, 1972 The Blood-Brain Barrier, in: The Structure and Function of Nervous Tissue. Academic Press, New York, New York, p. 542.

Briaire JJ, Frijns JHM, 2006 The consequences of neural degeneration regarding optimal cochlear implant position in scala tympani: A model approach. Hearing Research 214, 17–27. 10.1016/j.heares.2006.01.015 [PubMed: 16520009]

Butson CR, Miller IO, Normann RA, Clark GA, 2011 Selective neural activation in a histologically derived model of peripheral nerve. Journal of Neural Engineering 8, 036009 10.1088/1741-2560/8/3/036009 [PubMed: 21478574]

Camilleri M, Toouli J, Herrera MF, Kulseng B, Kow L, Pantoja JP, Marvik R, Johnsen G, Billington CJ, Moody FG, Knudson MB, Tweden KS, Vollmer M, Wilson RR, Anvari M, 2008 Intra-abdominal vagal blocking (VBLOC therapy): clinical results with a new implantable medical device. Surgery 143, 723–731. 10.1016/j.surg.2008.03.015 [PubMed: 18549888]

Carnevale NT, Hines ML, 2006 The NEURON Book. Cambridge University Press, Cambridge, UK.

Choi AQ, Cavanaugh JK, Durand DM, 2001 Selectivity of multiple-contact nerve cuff electrodes: a simulation analysis. IEEE Trans Biomed Eng 48, 165–172. 10.1109/10.909637 [PubMed: 11296872]

Cole K, Curtis H, 1936 Electric impedance of nerve and muscle. Cold Spring Harb Symp Quant Biol 4, 73–89.

Cole K, Li C, Bak A, 1969 Electrical Analogues for Tissues. Exp Neurol 24, 459–73. [PubMed: 5800962]

Cole KS, Hodgkin AL, 1939 Membrane and protoplasm resistance in the squid giant axon. J. Gen. Physiol 22, 671–687. [PubMed: 19873126]

Cranford JP, Kim BJ, Neu WK, 2012 Asymptotic model of electrical stimulation of nerve fibers. Med Biol Eng Comput 50, 243–251. 10.1007/s11517-012-0870-3 [PubMed: 22350436]

Curtis H, Cole K, 1938 Transverse electric impedance of the squid giant axon. J Gen Physiol 21, 757–65. [PubMed: 19873081]

Davson H, Kleeman C, Levin E, 1962 Quantitative studies of the passage of different substances out of the cerebro-spinal fluid. J Physiol 161, 126–142. [PubMed: 13883991]

Famm K, Litt B, Tracey KJ, Boyden ES, Slaoui M, 2013 Drug discovery: a jump-start for electroceuticals. Nature 496, 159–161. 10.1038/496159a [PubMed: 23579662]

Feng Z, Yu Y, Guo Z, Cao J, Durand DM, 2014 High frequency stimulation extends the refractory period and generates axonal block in the rat hippocampus. Brain Stimul 7, 680–689. 10.1016/j.brs.2014.03.011 [PubMed: 24938914]

Foster AJ, Erickson BJ, Bierk MD, 2010 Custom sized neural electrodes. 7822486.

Frieswijk TA, Smit JP, Rutten WL, Boom HB, 1998 Force-current relationships in intraneural stimulation: role of extraneural medium and motor fibre clustering. Med Biol Eng Comput 36, 422–430. [PubMed: 10198524]

Geddes LA, Baker LE, 1967a The specific resistance of biological material - A compendium of data for the biomedical engineer and physiologist. Med. Biol. Eng 5, 271–293. 10.1007/BF02474537 [PubMed: 6068939]

Geddes LA, Baker LE, 1967b The specific resistance of biological material—A compendium of data for the biomedical engineer and physiologist. Medical & Biological Engineering 5, 271–293. 10.1007/BF02474537 [PubMed: 6068939]

Giordano J, 2005 The Neurobiology of Nociceptive and Anti-nociceptive Systems. Pain Physician 8, 277–90. [PubMed: 16850085]

Goodall EV, Kosterman LM, Holsheimer J, Struijk JJ, 1995 Modeling study of activation and propagation delays during stimulation of peripheral nerve fibers with a tripolar cuff electrode. IEEE Transactions on Rehabilitation Engineering 3, 272–282. 10.1109/86.413200

Grill WM, Mortimer JT, 1994 Electrical properties of implant encapsulation tissue. Ann. Biomed. Eng 22, 23–33. 10.1007/BF02368219 [PubMed: 8060024]

Grinberg Y, Schiefer MA, Tyler DJ, Gustafson KJ, 2008 Fascicular perineurium thickness, size, and position affect model predictions of neural excitation. IEEE T. Neur. Sys. Reh 16, 572–581. 10.1109/TNSRE.2008.2010348

Guo Y-P, 1987 Pathological changes in the vagus nerve in diabetes and chronic alcoholism. J Neurol Neurosurg Psychiatry 50, 1449–53. [PubMed: 3694205]

Haberler C, Alesch F, Mazal PR, Pilz P, Jellinger K, Pinter MM, Hainfellner JA, Budka H, 2000 No tissue damage by chronic deep brain stimulation in Parkinson's disease. Ann. Neurol 48, 372–376. [PubMed: 10976644]

Helmers S, 2012 Application of a computational model of vagus nerve stimulation. Acta Neurol Scand 126, 336–43. [PubMed: 22360378]

Howell B, Huynh B, Grill WM, 2015 Design and in vivo evaluation of more efficient and selective deep brain stimulation electrodes. J Neural Eng 12, 046030 10.1088/1741-2560/12/4/046030 [PubMed: 26170244]

Kawagishi K, 2008 Tyrosine hydroxylase immunoreactive fibers in human vagus nerve. J Clin Neurosci 15, 1023–6. [PubMed: 18617399]

Kawagishi K, Fukushima N, Yokouchi K, Sumitomo N, Kakegawa A, Moriizumi T, 2008 Tyrosine hydroxylase-immunoreactive fibers in the human vagus nerve. J. Clin. Neurosci 15, 1023–1026. 10.1016/j.jocn.2007.08.032 [PubMed: 18617399]

Kilgore KL, Bhadra N, 2014 Reversible nerve conduction block using kilohertz frequency alternating current: reversible KHFAC nerve block. Neuromodulation 17, 242–255. 10.1111/ner.12100 [PubMed: 23924075]

Lempka SF, McIntyre CC, Kilgore KL, Machado AG, 2015 Computational Analysis of Kilohertz Frequency Spinal Cord Stimulation for Chronic Pain Management. Anesthesiology 122, 1362–1376. 10.1097/ALN.0000000000000649 [PubMed: 25822589]

Martin-Portugues I, 2005 Histopathologic features of the vagus nerve after electrical stimulation in swine. Histol Histopath 20, 851–856.

McGee MJ, Grill WM, 2016 Modeling the spinal pudendo-vesical reflex for bladder control by pudendal afferent stimulation. J Comput Neurosci 40, 283–296. 10.1007/s10827-016-0597-5 [PubMed: 26968615]

McIntyre C, Grill W, 2000 Selective Microstimulation of Central Nervous System Neurons. Ann Biomed Eng 28, 219–33. [PubMed: 10784087]

McIntyre C, Richardson A, Grill W, 2002 Modeling the excitability of mammalian nerve fibers: influence of afterpotentials on the recovery cycle. J Neurophysiol 87, 995–1006. [PubMed: 11826063]

McIntyre CC, Grill WM, Sherman DL, Thakor NV, 2004 Cellular effects of deep brain stimulation: model-based analysis of activation and inhibition. J. Neurophysiol 91, 1457–1469. 10.1152/jn.00989.2003 [PubMed: 14668299]

McNeal DR, 1976 Analysis of a model for excitation of myelinated nerve. IEEE T. Biomed. Eng BME-23, 329–337. 10.1109/TBME.1976.324593

Meffin H, Tahayori B, Grayden DB, Burkitt AN, 2012 Modeling extracellular electrical stimulation: I. Derivation and interpretation of neurite equations. Journal of Neural Engineering 9, 065005 10.1088/1741-2560/9/6/065005 [PubMed: 23187045]

Meffin H, Tahayori B, Sergeev EN, Mareels IMY, Grayden DB, Burkitt AN, 2014 Modelling extracellular electrical stimulation: III. Derivation and interpretation of neural tissue equations. Journal of Neural Engineering 11, 065004 10.1088/1741-2560/11/6/065004 [PubMed: 25419585]

Mei N, Condamin M, Boyer A, 1980 The composition of the vagus nerve of the cat. Cell Tissue Res. 209, 423–431. 10.1007/BF00234756 [PubMed: 7407841]

Moss J, Ryder T, Aziz TZ, Graeber MB, Bain PG, 2004 Electron microscopy of tissue adherent to explanted electrodes in dystonia and Parkinson's disease. Brain 127, 2755–2763. 10.1093/brain/awh292 [PubMed: 15329356]

Nicholson PW, 1965 Specific impedance of cerebral white matter. Exp. Neurol 13, 386–401. [PubMed: 5847284]

Pelot NA, Behrend C, Grill W, 2017 Modeling the response of small myelinated axons in a compound nerve to kilohertz frequency signals. Journal of Neural Engineering. 10.1088/1741-2552/aa6a5f

Pelot NA, Thio BJ, Grill WM, 2018 Modeling Current Sources for Neural Stimulation in COMSOL. Frontiers in Computational Neuroscience 12 10.3389/fncom.2018.00040

Prechtl JC, Powley TL, 1990 The fiber composition of the abdominal vagus of the rat. Anat. Embryol 181, 101–115. 10.1007/BF00198950 [PubMed: 2327594]

Ranck JB Jr, Bement SL, 1965 The specific impedance of the dorsal columns of cat: an anisotropic medium. Exp. Neurol 11, 451–463. [PubMed: 14278100]

Rao GS, 1978 A note on the limb nerves of the frog (Rana tigrina). Anat Anz 143, 152–155. [PubMed: 646124]

Raspopovic S, Petrini FM, Zelechowski M, Valle G, 2017 Framework for the Development of Neuroprostheses: From Basic Understanding by Sciatic and Median Nerves Models to Bionic Legs and Hands. Proceedings of the IEEE 105, 34–49. 10.1109/JPROC.2016.2600560

Robinson H, 1972 A Study of the Capacity of Myelinated and Unmyelinated Nerves to Induce Experimental Allergic Neuritis. Acta Neuropath. 21, 99–108. [PubMed: 5054702]

Roth BJ, Gielen FLH, 1987 A comparison of two models for calculating the electrical potential in skeletal muscle. Annals of Biomedical Engineering 15, 591–602. 10.1007/BF02364251 [PubMed: 3688587]

Sarr MG, Billington CJ, Brancatisano R, Brancatisano A, Toouli J, Kow L, Nguyen NT, Blackstone R, Maher JW, Shikora S, Reeds DN, Eagon JC, Wolfe BM, O'Rourke RW, Fujioka K, Takata M, Swain JM, Morton JM, Ikramuddin S, Schweitzer M, Chand B, Rosenthal R, 2012 The EMPOWER study: randomized, prospective, double-blind, multicenter trial of vagal blockade to induce weight loss in morbid obesity. Obes. Surg 22, 1771–1782. 10.1007/s11695-012-0751-8 [PubMed: 22956251]

Schiefer MA, Triolo RJ, Tyler DJ, 2008 A model of selective activation of the femoral nerve with a flat interface nerve electrode for a lower extremity neuroprosthesis. IEEE Trans Neural Syst Rehabil Eng 16, 195–204. 10.1109/TNSRE.2008.918425 [PubMed: 18403289]

Schiefer MA, Tyler DJ, Triolo RJ, 2012 Probabilistic modeling of selective stimulation of the human sciatic nerve with a flat interface nerve electrode. J Comput Neurosci 33, 179–190. 10.1007/s10827-011-0381-5 [PubMed: 22222951]

Stolinski C, 1995 Structure and composition of the outer connective tissue sheaths of peripheral nerve. J. Anat 186 (Pt 1), 123–130. [PubMed: 7649808]

Tahayori B, Meffin H, Sergeev EN, Mareels IMY, Burkitt AN, Grayden DB, 2014 Modelling extracellular electrical stimulation: IV. Effect of the cellular composition of neural tissue on its spatiotemporal filtering properties. Journal of Neural Engineering 11, 065005 10.1088/1741-2560/11/6/065005 [PubMed: 25419652]

Tailai Z, Junsheng T, Zuxun Z, Baokang Z, Yunping M, 1980 Vagus nerve anatomy at the lower esophagus and stomach. Chinese Med. J-Peking 93, 629–636.

Tasaki I, 1955 New Measurements of the Capacity and the Resistance of the Myelin Sheath and the Nodal Membrane of the Isolated Frog Nerve Fiber. Am J Physiol 181, 639–50. [PubMed: 13238615]

Topp K, Boyd B, 2006 Structure and Biomechanics of Peripheral Nerves: Nerve Responses to Physical Stresses and Implications for Physical Therapist Practice. Phys Ther 86, 92–109. [PubMed: 16386065]

Tweden K, 2013 Email Correspondence: Cross Sections through juvenile porcine intra-abdominal vagus nerve from EnteroMedics Inc.

Waataja J, 2011 Effects of high-frequency alternating current on axonal conduction through the vagus nerve. J Neural Eng 8, 056013. [PubMed: 21918293]

Weerasuriya A, Spangler RA, Rapoport SI, Taylor RE, 1984 AC impedance of the perineurium of the frog sciatic nerve. Biophys. J 46, 167–174. 10.1016/S0006-3495(84)84009-6 [PubMed: 6332648]

Williams PE, Lowry A, Hill R, Masson E, 2000 Relationship between fascicle size and perineurial collagen IV content in diabetic and control human peripheral nerve. Histopathology 36, 551–555. [PubMed: 10849098]

Wongsarnpigoon A, Grill WM, 2010 Energy-efficient waveform shapes for neural stimulation revealed with a genetic algorithm. Journal of Neural Engineering 7, 046009 10.1088/1741-2560/7/4/046009 [PubMed: 20571186]

Zhang K, Sejnowski T, 2000 A universal scaling law between gray matter and white matter of cerebral cortex. Proc Natl Acad Sci USA 97, 5621–6. [PubMed: 10792049]

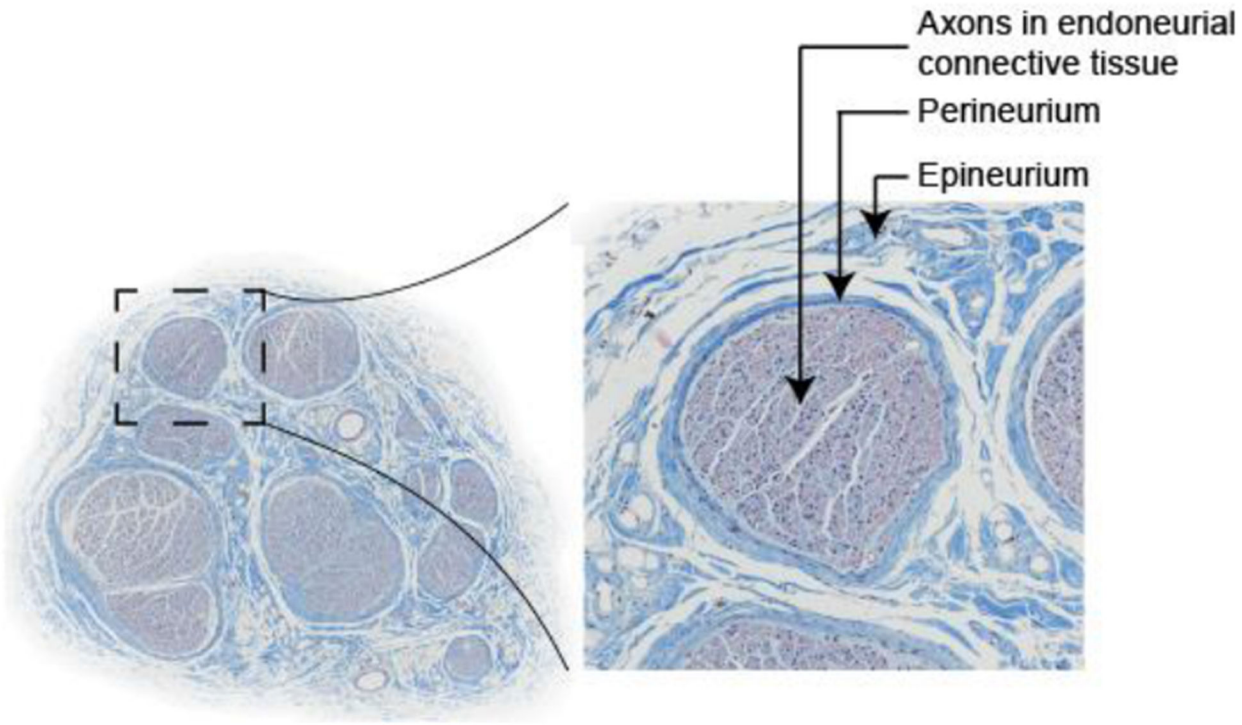

Figure 1.

Cross section of human cervical vagus nerve stained with Masson's trichrome, comprised of fascicles embedded in epineurial connective tissue. Each fascicle is ensheathed in perineurium. Each fascicle is composed of a bundle of axons in endoneurial connective tissue, typically modeled as a homogenized anisotropic bulk endoneurial tissue.

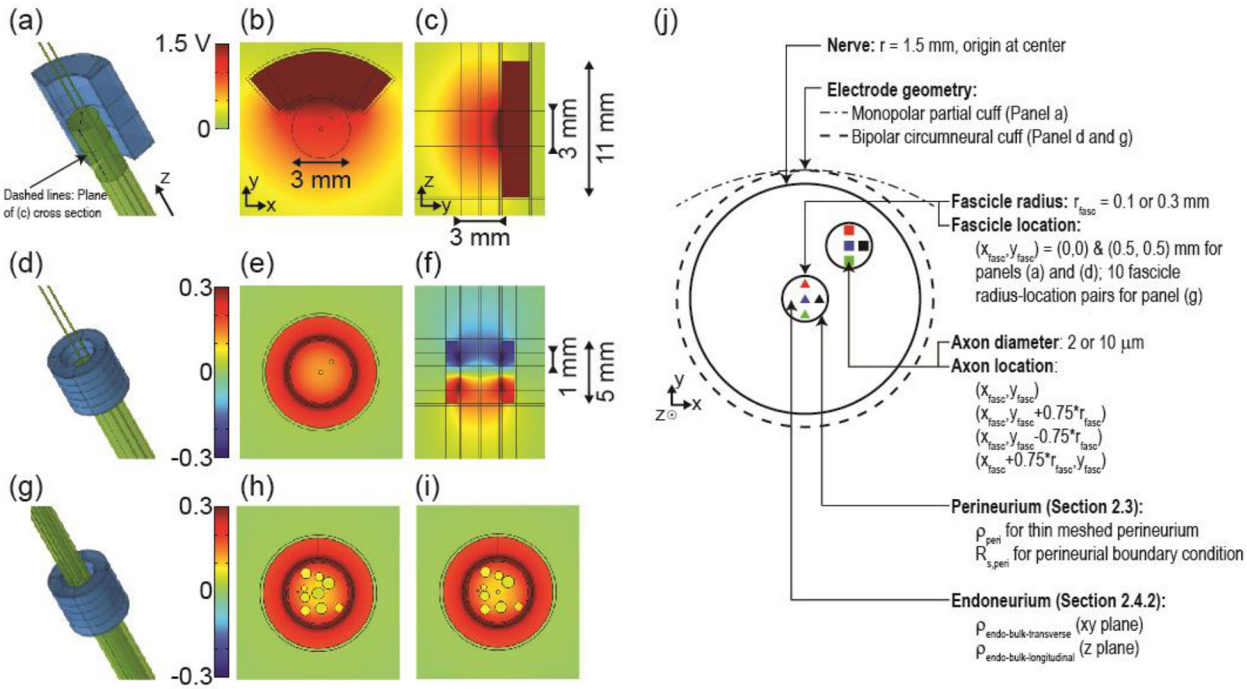

Figure 2.

(a, d, g) Three-dimensional finite element models of compound nerves (two fascicles (a and d) or 10 fascicles (g)) with a monopolar partial cuff electrode (a) or with a bipolar circumneural cuff electrode (d and g). (b, e, h, i) Transverse cross sections showing the cuff electrode around the nerve containing two small fascicles (0.1 mm radius) or 10 fascicles (0.3 and 0.1 mm radii for the centre fascicle in panels (h) and (i), respectively). The cross section in panel (b) is through the centre of the single electrode contact. The cross sections in panels (e), (h), and (i) are through the centre of the bottom electrode contact. (c and f) Longitudinal cross sections showing vertical extent of cuff electrodes. Orientation of longitudinal cross sections is indicated with dashed lines on panel (a). Potential distributions are shown in response to 1 mA monopolar stimulus or +1 mA & −1 mA bipolar stimulus. Note the different colour axis bounds for the two electrode designs, with matched colours for 0 V. (j) Schematic of the FEM cross section outlining the parameters examined in the perineurium and endoneurium resistivity studies. Note that in the perineurium studies with simplified nerve geometry, we only modeled the centre fascicle.

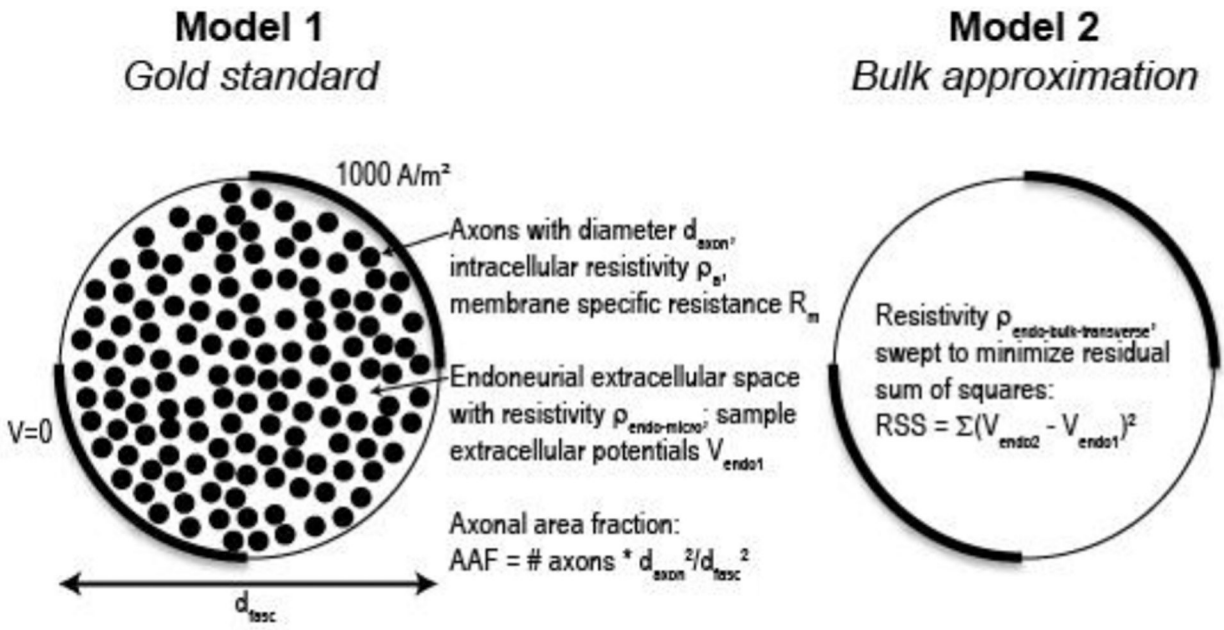

Figure 3.
Schematic of methods for numerical estimation of bulk transverse endoneurial resistivity.

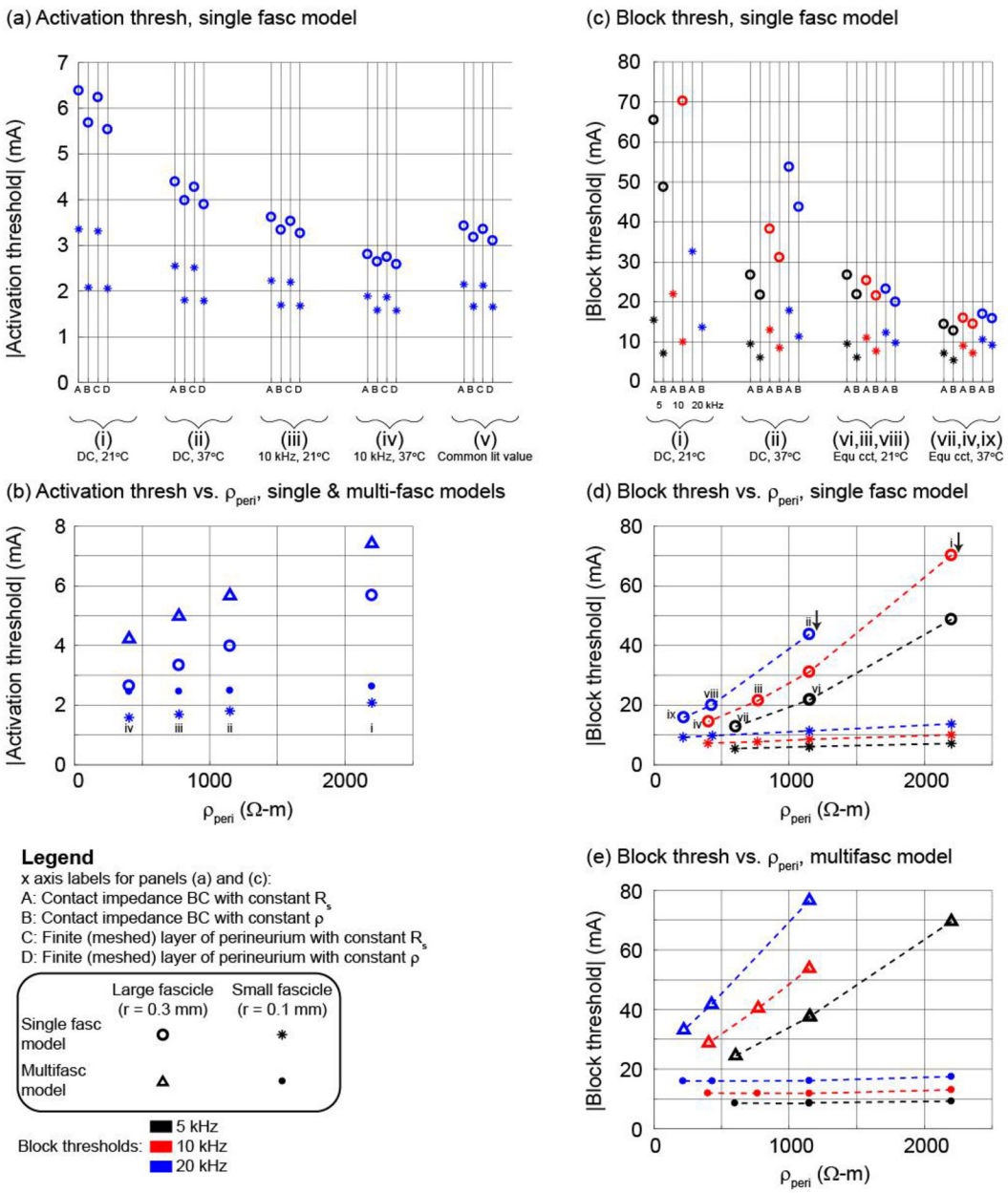

Figure 4.

Using the bipolar circumferential cuff and a 2 μm axon in the centre of the middle fascicle (see illustration of methods in Figure 2), thresholds for activation ((a) and (b)) and block ((c) to (e)) with different representations of the perineurium (x axis labels A to D) and estimates of perineurium resistivity (i to ix; see Table 2). Panels (b), (d), and (e) show the Method B data (constant ρ). Panels (a), (c), and (d) show thresholds for the single fascicle model. Panel (b) shows thresholds for the single fascicle and multifascicular nerve models. Panel (e) shows thresholds for the multifascicular model; the labels i to viii in panel (d) also apply to panel (e). Results for other electrode designs, fibre diameters, fascicles, and axon locations are provided in Supplement D.

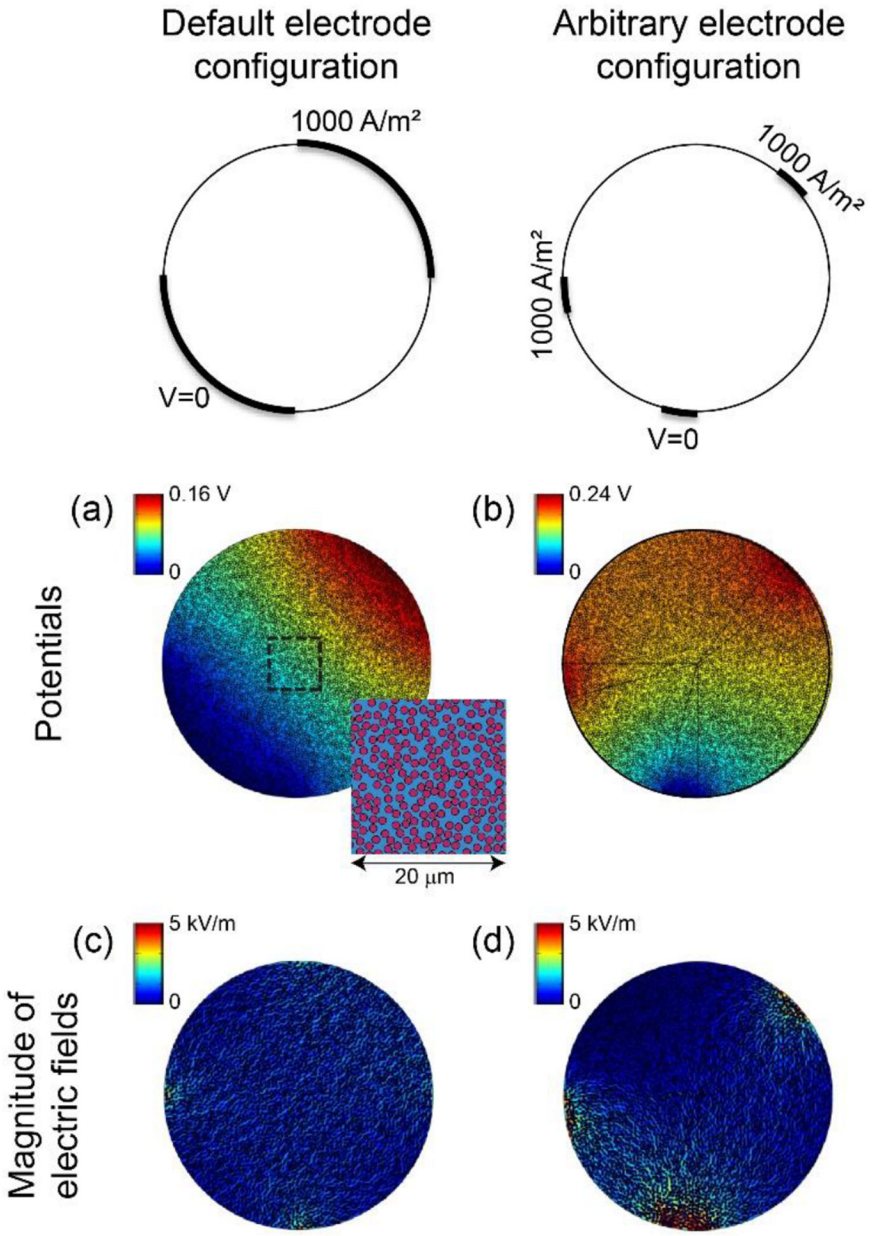

Figure 5.

Potential distributions ((a) and (b)) and magnitude of electric fields ((c) and (d)) for two electrode configurations with 2D FEM of fascicle with individually-modeled axons (Figure 3). Inset in panel (a) shows fibre packing within dashed box. The colour map of the electric fields spanning 0 to 5 kV/m is the same as Figure 6 to permit direct visual comparison.

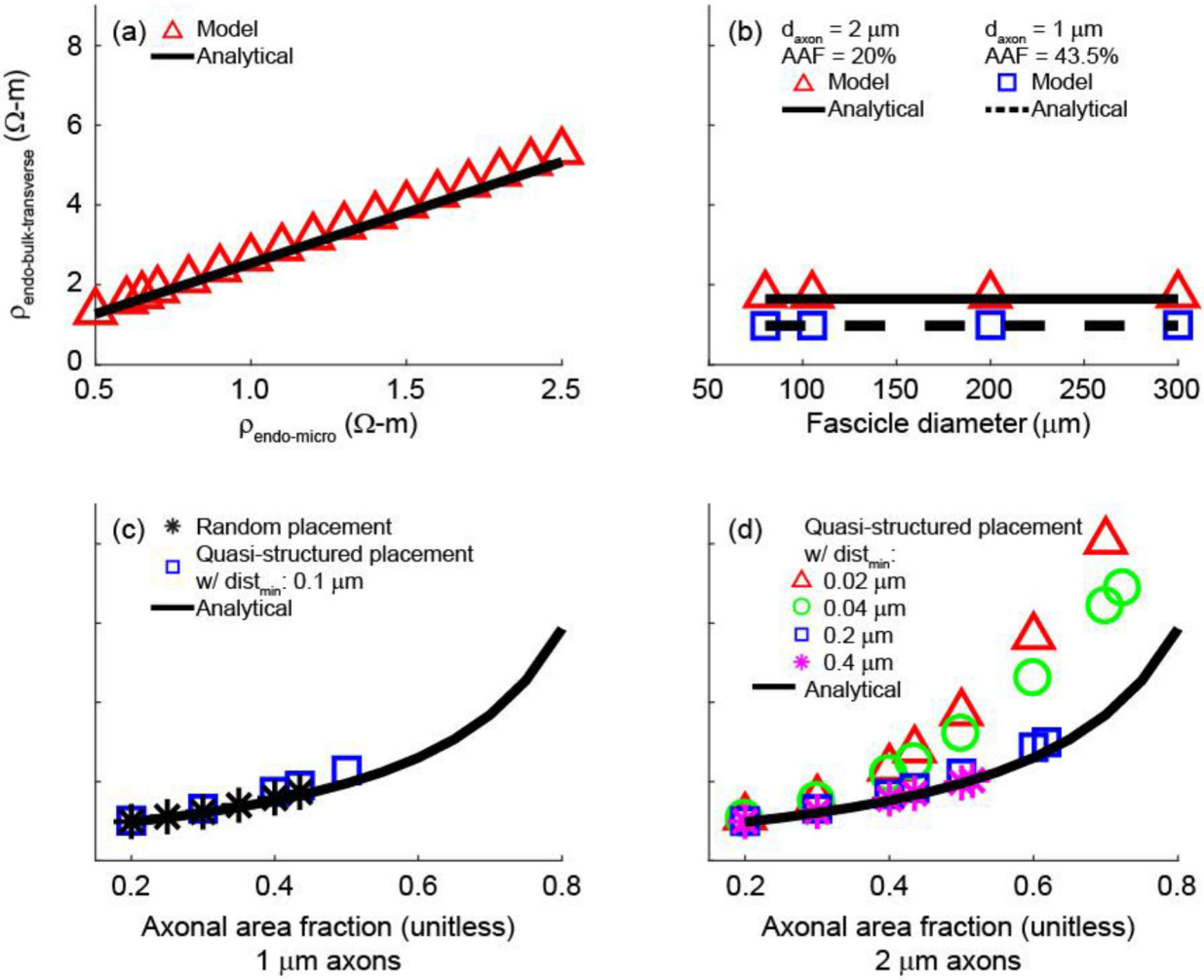

Figure 6.

Values of $\rho_{endo\text{-}bulk\text{-}transverse}$ obtained with the model and the analytical expression as a function of $\rho_{endo\text{-}micro}$ (a), fascicle diameter (b), and AAF (c and d). In (a), we used the default parameters of 1 μm axons, AAF = 43.5%, and $dist_{min}$ = 0.1 μm. In the AAF sweep with 1 μm axons (c), $\rho_{endo\text{-}bulk\text{-}transverse}$ was evaluated for random axon placement, quasi-structured axon placement, and the analytical expression. In the AAF sweep with 2 μm axons (d), we evaluated $\rho_{endo\text{-}bulk\text{-}transverse}$ for quasi-structured placement with four different minimum inter-axonal distances ($dist_{min}$), as well as the analytical expression.

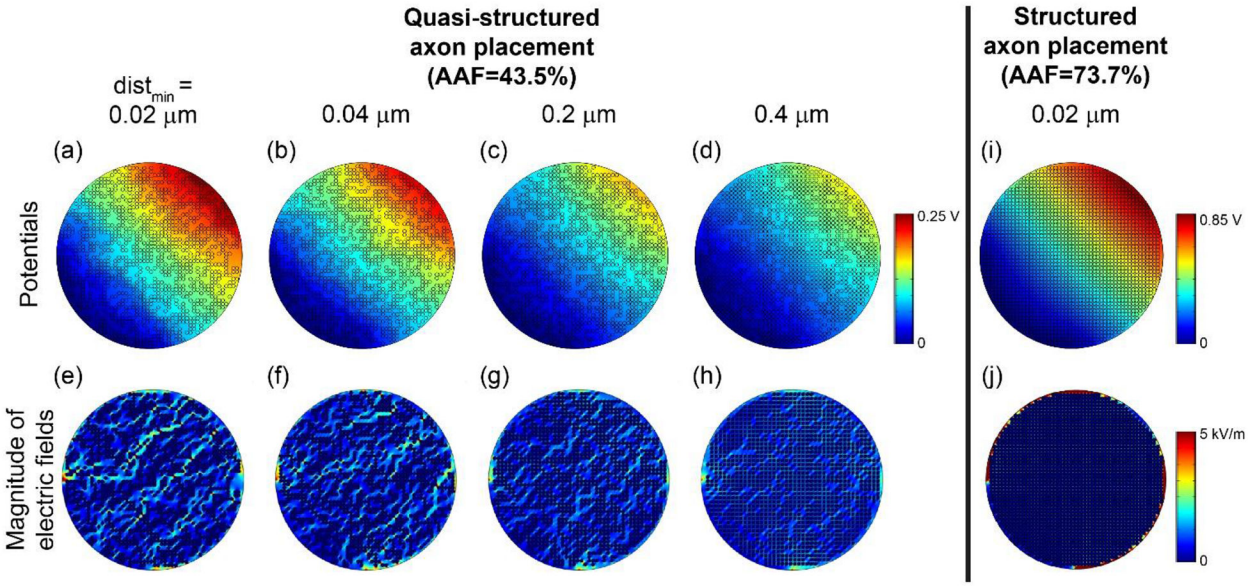

Figure 7.

Potential distributions (top row) and electric field magnitudes (bottom row) with increasing minimum distance ($dist_{min}$) between object boundaries (from (a) to (d) and (e) to (h)). In all cases, we initially placed 2 μm axons in a grid formation in a 105 μm fascicle ((i) and (j)). Then, we randomly removed axons to achieve AAF = 43.5%. The colour map of the electric fields spanning 0 to 5 kV/m is the same as Figure 5 to permit direct visual comparison.

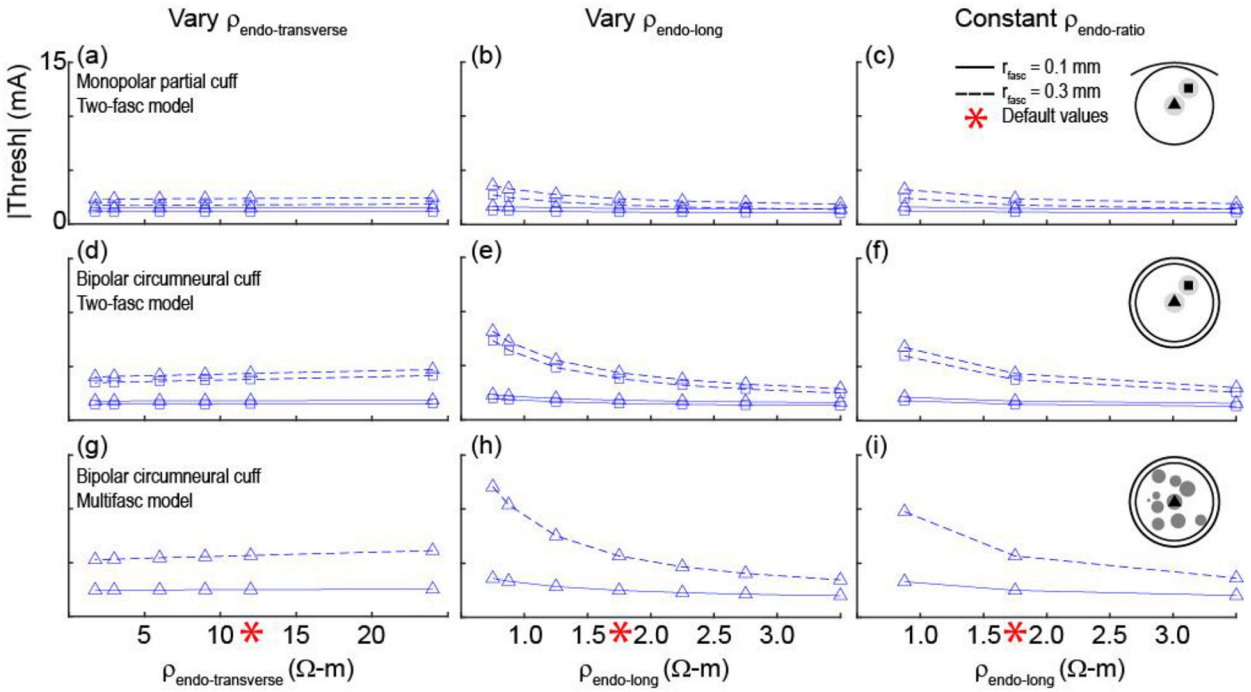

Figure 8.

Activation thresholds for axons in 3D FEMs of nerves and cuff electrodes across different values of endoneurial resistivity (see illustration of methods in Figure 2). The default resistivities (red asterisks) were 12 Ω-m for $\rho_{endo\text{-}transverse}$ and 1.75 Ω-m for $\rho_{endo\text{-}long}$. In the last column, the ratio of the transverse resistivity to the longitudinal resistivity was constant at 12 Ω-m/1.75 Ω-m = 6.9. All simulations used 2 μm axons and ρ_{peri} = 1149 Ω-m (DC, 37°C). First and second rows: Thresholds for the nerve model with two fascicles for different cuff electrode geometries. Third row: Thresholds for the nerve model with 10 fascicles and the bipolar circumneural cuff geometry. Data with four axon locations per fascicle – with the addition of thresholds for 2 and 10 μm axons placed in all fascicles of the multifascicular model – are provided in Supplement F.

Table 1.

Default geometrical and electrical parameters of the finite element models. The geometrical parameters for the bipolar circumneural cuff electrode are provided in the text. Changes in the values are indicated with the associated results. Modified from (Pelot et al., 2017).

Geometrical Parameters: ***Nerve***				***mm unless otherwise indicated***
Height	**Radii**			
	Medium	**Epineurium/Nerve**	**Endoneurium/Fascicle**	
100	20	1.5 (Tailaietal., 1980)	Simplified nerve: 0.3 (Kawagishi et al., 2008) or 0.1 Multifascicular nerve: 0.05 to 0.3 (unpublished data)	

Geometrical Parameters: ***Monopolar partial cuff electrode***				***mm unless otherwise indicated***
	Height	**Radius**	**Thickness**	**Subtending angle (deg.)**
Electrode substrate (Camilleri et al., 2008; Foster et al., 2010)	10.8	3.2	2.2	**63**
Electrode contact (Camilleri et al., 2008; Foster et al., 2010)	2.8	3.2	**N/A**	**83**

Electrical Parameters				***Ω-m unless otherwise indicated***
Medium	**Encapsulation tissue**	**Epineurium**	**Perineurium**	**Endoneurium**
30 (Geddes and Baker, 1967a)	6.3 (Grill and Mortimer, 1994)	6.3 (Grill and Mortimer, 1994; Stolinski, 1995)	1149 Ω-m * 0.03 * d_{fasc} (Grinberg et al., 2008; Weerasuriya et al., 1984)	1.75 longitudinal 12 transverse (Ranck and Bement, 1965)

Table 2.

Nine estimates (i to ix) and four methods (A, B, C, D) for representing the perineurium. “Constant” refers to constancy from Weerasuriya’s frog sciatic nerve measurements to our model, as well as across fascicles diameters in our model. Small fascicle: r = 0.1 mm; large fascicle: r = 0.3 mm. R_s: sheet resistance; ρ: resistivity. When using Method B with the multifascicular model, we used the resistivity from Method D, and multiplied by the perineurium thickness estimated as 3% of each fascicle’s diameter.

		Sheet resistance for perineurial thin film approximation (Ω-m^2)			Resistivity of finite (meshed) layer of perineurium (Ω-m)		
		Constant R_s	Constant ρ		Constant R_s		Constant ρ
		A	B – Small fascicle	B – Large fascicle	C – Small fascicle	C – Large fascicle	D
i	DC, 21°C	0.0478	0.0132	0.0396	7967	2656	2198
ii	DC, 37°C	0.0250	0.0069	0.0207	4164	1388	1149
iii	10 kHz, 21°C	0.0168	0.0046	0.0139	2800	933	772
iv	10 kHz, 37°C	0.0088	0.0024	0.0073	1464	488	404
V	Common value in lit	0.0149	0.0041	0.0123	2483	828	685
vi	5 kHz, 21°C	0.0251	0.0069	0.0208	--	--	1154
vii	5 kHz, 37°C	0.0131	0.0036	0.0109	--	--	603
viii	20 kHz, 21°C	0.0094	0.0026	0.0077	--	--	430
ix	20 kHz, 37°C	0.0049	0.0013	0.0040	--	--	225

Table 3.

Model parameters to estimate the bulk transverse endoneurial resistivity for a bundle of unmyelinated axons.

Parameter (variable name)	Default value	Test range	References
Fascicle diameter (df_{asc})	105 μm	80–300 μm	(Kawagishi, 2008; Tweden, 2013)
Axon diameter (d_{axon})	1 μm	0.5–2 μm	(Giordano, 2005; Guo, 1987; Helmers, 2012; Mei et al., 1980; Robinson, 1972; Waataja, 2011)
Axonal area fraction (AAF)[a]	0.435[b]	0.20–0.737[c]	(Agostini, 1957; Altman and Plonsey, 1989)
Endoneurial resistivity ($\rho_{endo\text{-}micro}$)	0.65 Ω-m	0.5–2 Q-m	(Altman and Plonsey, 1989; Geddes and Baker, 1967b)
Intracellular resistivity (ρ_a)	0.7 Ω-m	0.5–4 Q-m	(McIntyre et al., 2002; McIntyre and Grill, 2000)
Specific membrane resistance (R_m)	0.2 Ω-m^2	0.0025–0.4 Ω-m^2 [d]	(Barrett and Crill, 1974; Cole and Hodgkin, 1939)

[a] Table 5 (Supplement C) shows calculations for estimating the axonal area fraction for a single fascicle based on cat posterior abdominal vagus nerve morphology.

[b] Although we estimated an axonal area fraction of 0.45 from cat posterior abdominal vagus nerve histology slides (Table 5, Supplement C), we could only achieve $AAF = 0.435$ in the finite element model with the default parameters.

[c] The lower bound of this range was chosen arbitrarily simply to test model sensitivity to this parameter. The upper bound is the maximum extent to which we could pack 2 μm axons into a 105 μm diameter fascicle.

[d] The lower bound of this range represents the minimum membrane resistance for squid giant axon if all axons in the fascicle are active simultaneously.